Supplementary Materials

Controllable dielectric elastomer actuators for centimeter-scale flexible underwater robot

Yali Zhang[1,#], Chen Zhang[1,#], Chenyu Zhang[1,2], Junhao Shi[1], Juntian Qu[1,*], Xiang Qian[1,*]

[1]Shenzhen International Graduate School, Tsinghua University, Shenzhen 518055, Guangdong, China.
[2]Sibley School of Mechanical and Aerospace Engineering, Cornell University, Ithaca, NY 14850, USA.
[#]Authors contributed equally to this work.

[*]**Correspondence to:** Prof. Xiang Qian, Prof. Juntian Qu, Shenzhen International Graduate School, Tsinghua University, Shenzhen 518055, Guangdong, China. E-mail: qian.xiang@sz.tsinghua.edu.cn; juntian.qu@sz.tsinghua.edu.cn

Supplementary Note 1. Specific models of materials and equipment used in the DEA fabrication process.

Supplementary Table 1. Specific models of materials and equipment used in the DEA fabrication process

Category	Specific Model
Silicone Rubber	Zhermack ZA 8 LT
SWCNTs	OCSiAl TUBALL BATT H_2O 0.4%
Masking Film	25μm PET Film(Tiantai Mubai E-commerce Co., Ltd.)
Mask Cutter	Silhouette CAMEO5 Alpha
Dispersant	Aladdin Isopropanol (IPA)
Spin Coater	SETCAS KW-4BC-1
Centrifuge	Eppendorf 5430R
PTFE Filter Membrane	ADVANTEC 142 mm, 0.2 μm
Silicone Rubber for Bonding	Kafuter 704
Defoaming Mixer	Thinky AR-100

Supplementary Note 2. Experimental setup and detailed procedures for DEA bending tests in air and aqueous media.

This note supplements the detailed experimental setup, test procedures, insulation and waterproof packaging strategy for bending angle measurement of planar-type and rolled-type dielectric elastomer actuators (DEAs) in air and aqueous media, which is the key experimental basis for the bending performance characterization of DEAs in the main text. The core experimental devices, test processes and characterization results are shown in Supplementary Table 2 and Supplementary Figures 1-3, respectively.

2.1 Core Experimental Devices and Specifications

The core devices used for bending angle measurement of the two configurations of DEAs are consistent, and the specific models and specifications of the key components are summarized in Supplementary Table 2.

Supplementary Table 2. Core experimental devices and specifications for bending angle measurement

Device Name	Model/Specification
Full-bridge bending strain gauge	RunesKee-BF350-3EB
Fast-drying AB adhesive	Gelvany 302 Fast-drying AB adhesive
Epoxy Conductive AB Adhesive	SINWE 6529
Silicone rubber for bonding constraint layers and sealing	Kafuter 704
Waterproof Encapsulation Silicone Rubber	Ecoflex-0030AB
Full-bridge acquisition module	RunesKee
Data acquisition (DAQ) card	NI6009
High-voltage amplifier	Aigtek ATA-7020

2.2 Experimental Setup and Test Procedure in Air Medium

The bending angle measurement of DEAs in air medium was implemented through strain gauge sensing combined with programmed voltage driving, and the specific experimental steps are as follows:

Constraint Layer Bonding: A 25μm thick PTE film was bonded to one side of the DEA using Kafuter 704 silicone rubber.

Strain gauge bonding and DEA fixation: The full-bridge bending strain gauge was firmly bonded to the constrained layer surface of the prepared DEA using Gelvany 302 fast-drying AB adhesive. One end of the DEA was rigidly fixed on a horizontal experimental platform to ensure the free end could bend and deform without mechanical obstruction [Supplementary Figure 1C].

Strain gauge calibration and signal conversion: The bending angle change of the DEA was converted into a resistance change by the strain gauge. The full-bridge acquisition module collected the resistance change and further converted it into a voltage change in the range of -3 V ~ 4 V [Supplementary Figure 1B]. The quantitative calibration relationship between the DEA bending angle and the output voltage of the acquisition module was established, and the calibration results are shown in Supplementary Figure 2.

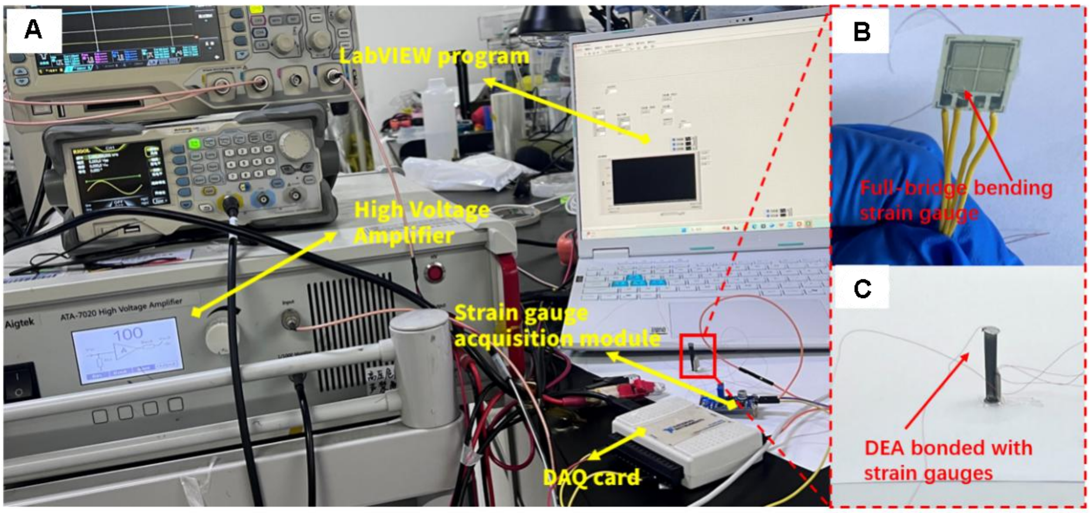

Supplementary Figure 1. (A) Calibration curve of bending angle and output voltage of strain gauge; (B) Schematic diagram of air medium bending angle measurement experimental setup; (C) Schematic diagram of DEA hierarchical insulation and waterproof packaging process.

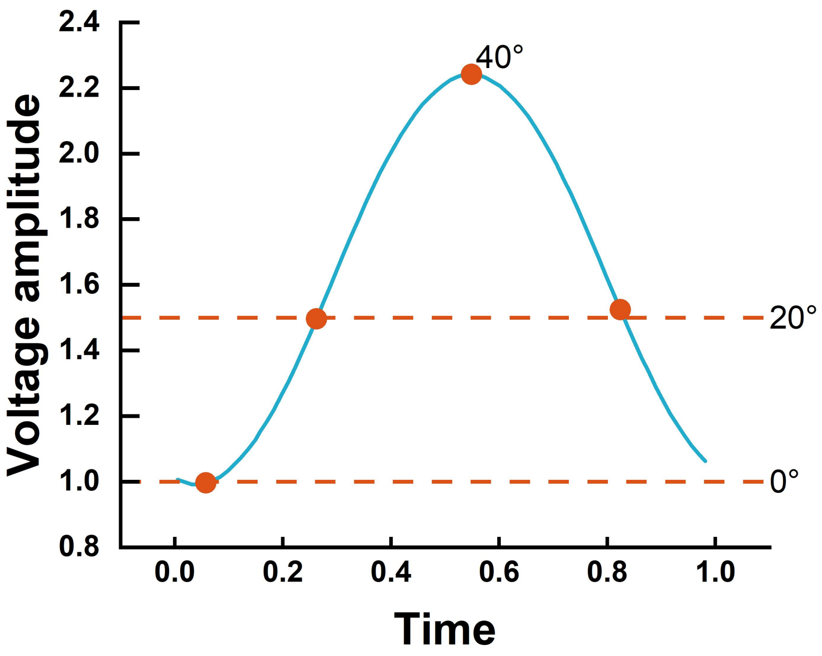

Supplementary Figure 2. Strain Gauge Calibration Results.

Driving voltage loading and bending angle acquisition: A LabVIEW program was used to generate and output an analog voltage of 0 ~ 5 V, which was transmitted through the output port of the NI6009 DAQ card and amplified 100 ~ 120 times by the Aigtek ATA-7020 high-voltage amplifier before being applied to the two ends of the DEA [Supplementary Figure 1A]. Combined with the aforementioned calibration relationship, the bending angle of the DEA free end under different driving voltages was collected and recorded in real time.

2.3 Insulation and Waterproof Packaging Strategy for Aqueous Medium

The test procedure and device connection mode for bending angle measurement in aqueous medium are completely consistent with those in air medium. To solve the key problems of electrical insulation for high-voltage loading and waterproofing for signal transmission underwater, a hierarchical insulation and waterproof packaging strategy was adopted for DEAs, and the specific operation steps are as follows:

Electrical connection: The electrical connection of the DEA was completed using SINWE6529 epoxy conductive AB adhesive to ensure good electrical conductivity and structural stability of the connection part.

Point-type sealing and insulation: The electrical connection part of the DEA and the signal connection part of the full-bridge bending strain gauge were sealed and insulated with Kraft 704 sealing silicone rubber, and left to stand for 24 h until complete curing to achieve waterproofing of key electrical parts.

Integral encapsulation: The DEA with completed point-type packaging was fully immersed in Ecoflex-0030 AB silicone rubber (A/B components mixed at 1:1 and defoamed), then taken out and cured for another 24 h to realize the full-surface insulation and waterproof encapsulation of the DEA. The schematic diagram of the entire packaging process is shown in Supplementary Figure 3C and Supplementary Figure 5.

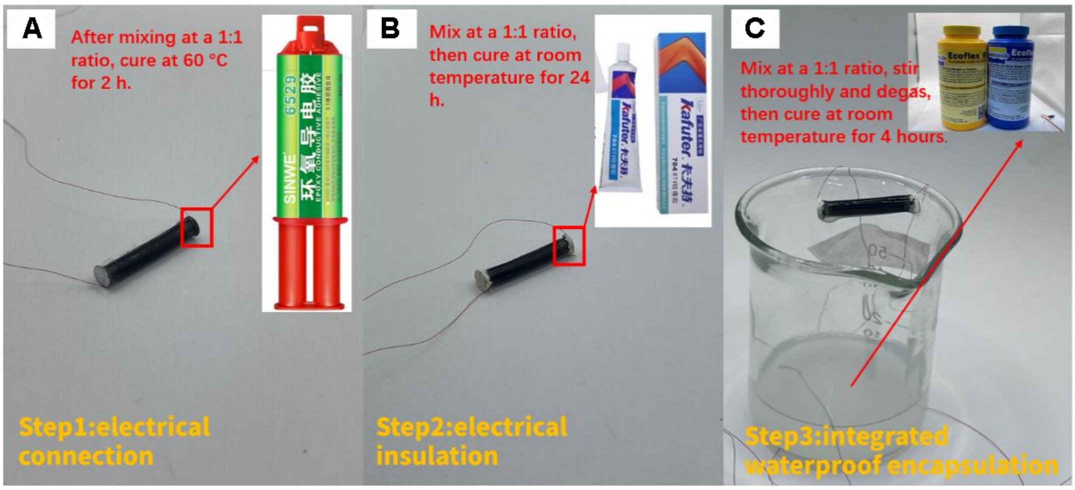

Supplementary Figure 3. Encapsulation Steps.

Underwater bending angle measurement: The fully encapsulated DEA was fixed on the experimental platform in a water tank, and the bending angle measurement was carried out according to the test procedure of the air medium, with the bending angle data collected and recorded in real time.

Supplementary Note 3. electrical model of DEA

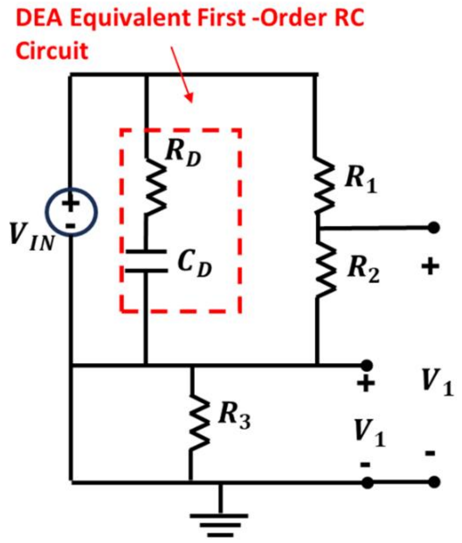

Supplementary Figure 4. Test circuit for testing first-order equivalent capacitance and resistance.

Supplementary Table 3. Electrical Parameters of the DEA based on the first-order RC circuit

Frequency	2HZ	20HZ	100HZ
Equivalent Resistance R_D	$2646\ k\Omega$	$998\ k\Omega$	$531.7\ k\Omega$
Equivalent Resistance C_D	$23.76nF$	$10nF$	$4.15nF$

Supplementary Table 4. Physical-to-Circuit Mapping

Circuit element	Meaning	Physical correspondence
C_D	Main effective capacitance of the actuator	Charge storage across the active electrode–dielectric overlap in the rolled multi structure (i.e., the portion of the stack that directly generates the driving electric field)
R_D	Lumped series loss resistance	Equivalent resistance contributed by compliant electrodes, HV leads, and electrode/lead contact interfaces (plus any distributed resistance along the rolled current path)
C_p	Additional non-ideal capacitive path not fully contributing to actuation	Stray/distributed capacitance arising from multilayer rolling (inter-layer fringe/overlap regions, micro air gaps/impurities), compact internal wiring (lead–lead and lead–electrode proximity), and measurement/setup stray capacitances

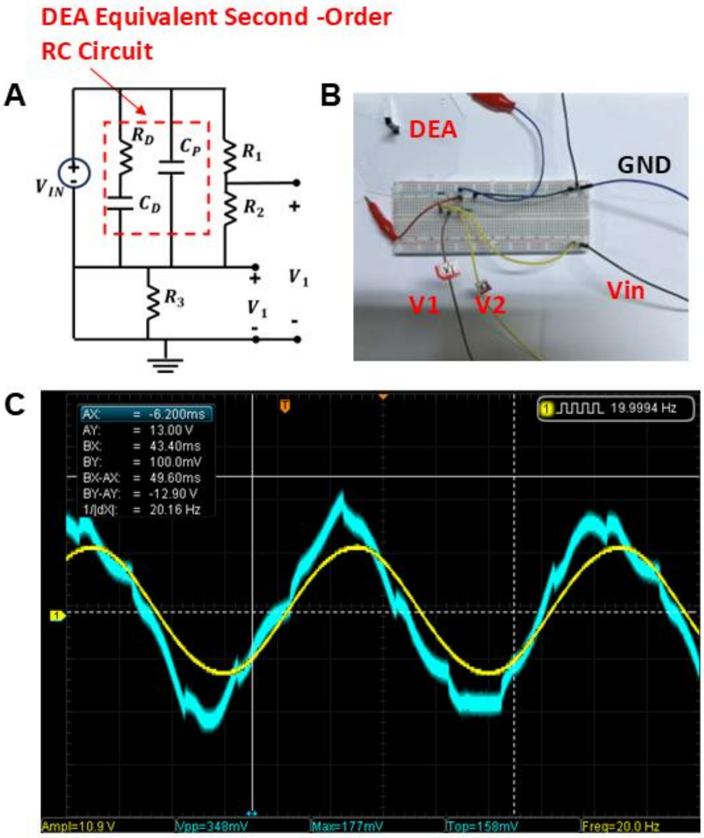

Supplementary Figure 5. (A) Test circuit for testing second-order equivalent capacitance and resistance. (B) Actually Built Test Circuit(C) Actually Measured Waveform.

$$G(S) = \frac{1 + SR_D C_D}{S^2 R_D C_D C_P + S(C_{P+} C_D)} \# \qquad (S1)$$

Supplementary Table 5. Electrical Parameters of the DEA based on the second-order RC circuit

Equivalent Resistance R_D	Equivalent Capacitance C_D	Total Parasitic Capacitance C_p
28.5 $k\Omega$	43.8 nF	0.1 nF

Supplementary Note 4 Mooney-Rivlin model with 5 parameters

Here, we adopt the derivation of the constitution model in reference[1]. Considering the three-dimensional main extension ratio λ_1, λ_2, λ_3, the first and second invariant of strain, denoted by I_1 and I_2, can be represented as:

$$I_1=\frac{\lambda_1^2+\lambda_2^2+2\lambda_3^2}{(\lambda_1\lambda_2\lambda_3)^{\frac{2}{3}}} \tag{S2}$$

$$I_2=\frac{\lambda_1^2\lambda_2^2+\lambda_2^2\lambda_3^2+\lambda_1^2\lambda_3^2}{(\lambda_1\lambda_2\lambda_3)^{\frac{4}{3}}} \tag{S3}$$

Then, Mooney-Rivlin model with 5 parameters can be described as:

$$W=C_{10}(I_1-3)+C_{01}(I_2-3)+C_{20}(I_1-3)^2+C_{02}(I_2-3)^2+C_{11}(I_1-3)(I_2-3) \tag{S4}$$

where W is the strain energy per unit of volume, and C_{10}, C_{01}, C_{20}, C_{02}, C_{11} are parameters to be determined.

To fit the parameters, we further consider the situation of uniaxial stretch of the isotropic materials, where

$$\lambda_1=\lambda,\lambda_2=\lambda_3=\frac{1}{\sqrt{\lambda}} \tag{S5}$$

Thus,

$$I_1=\lambda^2+\frac{2}{\lambda} \tag{S6}$$

and

$$I_2=\left(2\lambda+\frac{1}{\lambda^2}\right) \tag{S7}$$

The stress (σ) - strain (λ) relationship described by Mooney-Rivlin model with 5 parameters can be represented as:

$$\sigma=\frac{\partial W}{\partial\lambda}=\frac{\partial I_1}{\partial\lambda}[C_{10}+2C_{20}(I_1-3)+C_{11}(I_2-3)]+\frac{\partial I_2}{\partial\lambda}[C_{01}+2C_{02}(I_2-3)+C_{11}(I_1-3)] \tag{S8}$$

Where

$$\frac{\partial I_1}{\partial\lambda}=2(\lambda-\lambda^{-2}) \tag{S9}$$

$$\frac{\partial I_2}{\partial\lambda}=2(1-\lambda^{-3}) \tag{S10}$$

Finally, we can fit the model using experimental data.

Supplementary Table 6. Fitting Results of the Mooney-Rivlin model with 5 parameter

C_{10}	C_{01}	C_{20}	C_{02}	C_{11}
11142Pa	7767.5Pa	-27311Pa	40770Pa	3611.2Pa

Supplementary Note 5. Equivalent Bending Modulus

To avoid confusion, we denote the dimensionless bending strain by $\hat{\kappa}=z\kappa$(with z measured from the neutral surface), and use κ in the main text for curvature. Considering the assumption for bending motion in [Figure 4A], the main extension ratio can be defined as,

$$\lambda_1=1+\hat{\kappa},\lambda_2=1,\lambda_3=\frac{1}{1+\hat{\kappa}} \qquad (S11)$$

And

$$I\overset{\mathrm{def}}{=} I_1=I_2=(1+\hat{\kappa})^2+(\frac{1}{1+\hat{\kappa}})^2+1 \qquad (S12)$$

Thus, the strain energy can be rearranged as:

$$W=[C_{10}+C_{01}](I-3)+[C_{20}+C_{02}+C_{11}](I-3)^2 \qquad (S13)$$

To derive the equivalent bending modulus, we take the derivative of the above equation twice,

$$E_b=\frac{\partial\sigma}{\partial\hat{\kappa}}=\frac{\partial^2 W}{\partial\hat{\kappa}^2}=[C_{10}+C_{01}]\frac{\partial^2\mathrm{I}}{\partial\hat{\kappa}^2}+2[C_{20}+C_{02}+C_{11}]\left[\frac{\partial^2 I}{\partial\hat{\kappa}^2}(I-3)+\left(\frac{\partial I}{\partial\hat{\kappa}}\right)^2\right] \qquad (S14)$$

and further ignore the higher-order terms in above equation, E_b can be approximated as:

$$E_b\approx 8(C_{10}+C_{01}) \qquad (S15)$$

Supplementary Note 6 Explanation of scaling factor

1. Bending Moment Integration

Let the rolled DEA be modeled as a cylindrical shell with radius R and effective wall thickness t. The driving voltage V generates a uniform Maxwell stress $\sigma_{Maxwell}$ within the shell wall. The constraint layer is located at the bottom of the cylinder (at θ=0), defining the bending Neutral Axis.

For a differential element $dA=tRd\theta$ on the shell, its lever arm relative to the bottom constraint layer (the assumed rigid neutral axis) is $y(\theta)=R(1-\cos\theta)$.

The total active bending moment M_{rolled} generated by the rolled structure is obtained by integrating along the circumference:

$$M_{rolled}=\int_0^{2\pi}\sigma_{Maxwell}\cdot\ y(\theta)\cdot\ dA=\int_0^{2\pi}\sigma_{Maxwell}\cdot\ R(1-\cos\theta)\cdot\ (tRd\theta) \qquad (S16)$$

$$M_{rolled}=\sigma_{Maxwell}tR^2[\theta-\sin\theta]_0^{2\pi}=2\pi\sigma_{Maxwell}tR^2 \qquad (S17)$$

2. Flexural Stiffness Integration

According to the parallel axis theorem, the area moment of inertia I_{rolled} of the thin-walled cylindrical shell relative to the tangent at the bottom is:

$$I_{rolled}=\int_0^{2\pi}y(\theta)^2\cdot\ dA=\int_0^{2\pi}R^2(1-cos\,\theta)^2\cdot\ tRd\theta \qquad (S18)$$

$$I_{rolled}=tR^3\int_0^{2\pi}(1-2\cos\theta+\cos^2\theta)d\theta \qquad (S19)$$

Using the integral identity $\int_0^{2\pi}\cos^2\theta\,d\theta=\pi$,, we obtain:

$$I_{rolled}=tR^3(2\pi-0+\pi)=3\pi tR^3 \qquad (S20)$$

3. Theoretical Geometric Efficiency Factor

Based on the Euler-Bernoulli beam theory, the theoretical curvature κ_{rolled} of the rolled structure is:

$$\kappa_{rolled}=\frac{M_{rolled}}{EI_{rolled}}=\frac{2\pi\sigma tR^2}{E(3\pi tR^3)}=\frac{2}{3}\cdot\ \frac{\sigma}{ER} \qquad (S21)$$

In the equivalent planar model used in Equation (S21) of the main text, an ideal geometric transfer efficiency (where all material contributes to maximum bending efficacy) is assumed, corresponding to a normalized coefficient of 1.

Therefore, the Theoretical Geometric Efficiency Lower Bound of the rolled structure relative to the ideal planar model is:

$$\alpha_{theory}=\frac{2}{3}\approx 0.67 \tag{S22}$$

The theoretically derived $\alpha_{theory} = 0.67$ is based on the assumption of a perfectly rigid constraint (where the neutral axis is strictly fixed at the bottom).

In the actual device, the silicone adhesive connecting the DEA body and the PET constraint layer possesses a Finite Shear Modulus. This Non-ideal Constraint (or Partial Composite Action) allows for minute interlayer slip, causing the effective neutral axis to shift slightly upwards towards the centroid of the cross-section. This effect reduces the effective flexural stiffness I_{rolled}, thereby resulting in an actual curvature κ that is slightly higher than the prediction of the perfectly rigid model.

The experimentally measured coefficient 0.75 is very close to the theoretical value 0.67, with the difference (approximately 12%) reflecting the enhancement in bending performance due to the compliance of the adhesive layer. Therefore, 0.75 is a physical parameter that synthesizes the Cylindrical Geometric Distribution (the dominant factor, 2/3) and the Interlayer Shear Compliance (the secondary correction).

Supplementary Note 7. Validity of the Underwater Static Bending Model, Sources of Amplitude Reduction, and Calibration Protocol

In the underwater static (quasi-static) tests, the voltage is held constant at each level and the bending angle is recorded after it reaches a steady value, so $\dot{\theta}\approx 0$ and $\ddot{\theta}\approx 0$. The underwater rotational dynamics can be written as

$$M(V)-M_i(k)=D_h\,\dot{\theta}+(J+J_{\mathrm{add}})\ddot{\theta} \tag{S23}$$

Since the hydrodynamic damping and added-mass terms are velocity- and acceleration-dependent, they vanish at static equilibrium, yielding the static moment balance

$$M(V)=M_i(k) \tag{S24}$$

which remains valid for underwater static bending.

While the static equilibrium form is preserved, the underwater steady bending amplitude is observed to be smaller than that in air. This reduction can be attributed to underwater-induced static constraints and effective parameter shifts that decrease the effective actuation efficiency or structural compliance under the same applied voltage. Representative contributors include hydrostatic-pressure-related pre-stress and constraint effects, packaging- and immersion-induced changes in the effective electrical response, and environment-dependent variations in the effective mechanical properties of the material and structure. Over the tested voltage range, the combined influence is well represented as an overall amplitude scaling; therefore, a single multiplicative correction factor is adopted to calibrate the air-derived static model for underwater conditions without explicitly modeling each mechanism.

The multiplicative correction factor η_{uw} is identified using a calibration–validation protocol. The underwater quasi-static data are split into a calibration set and an independent validation set. η_{uw} is obtained on the calibration set by least-squares fitting implemented in MATLAB, and then directly applied to the validation set without further tuning. The relative error on the validation set is calculated at each voltage point as

$$e_i=\frac{\left|\theta_{exp}(V_i)-\theta_{pred}(V_i)\right|}{\theta_{exp}(V_i)} \tag{S25}$$

and the maximum value over all validation points remains below 10% across the tested voltage range (Figure 4C), supporting the robustness of the calibration. The identified factor is η_{uw}=0.6.

Supplementary Note 8. Derivation of the Underwater Open-Loop Transfer Function and Simulink Open-Loop Validation

According to the static electromechanical bending model in the main text, the electrostatic actuation moment is quadratic in the applied voltage:

$$M(V)=\frac{C_D(H^2-H_m^2)}{8hL}V^2\equiv\alpha V^2 \tag{S26}$$

where $\alpha=\frac{C_D\left(H^2-H_m^2\right)}{8hL}$.

Under the uniform-curvature assumption, the internal elastic restoring moment is linear in curvature:

$$M_i(k)=[E_cI_c+E_b(I-I_c)]k(t)\equiv K\,k(t) \tag{S27}$$

where $K=E_cI_c+E_b(I-I_c)$ is the equivalent bending stiffness coefficient. The curvature–angle relation satisfies

$$k(t)=\frac{\theta(t)}{L} \tag{S28}$$

Under underwater operating conditions, the bending motion is described by a second-order, control-oriented rotational dynamic model:

$$M(V)-M_i(k)=D\,\dot{\theta}(t)+J\,\ddot{\theta}(t) \tag{S29}$$

where D denotes the effective underwater damping coefficient and J denotes the effective underwater moment of inertia. Here, D and J are control-oriented equivalent parameters introduced to capture the dominant dynamic characteristics in a high-damping underwater environment.

To obtain the open-loop relationship from voltage squared to curvature, substituting the geometric relation $\theta(t)=Lk(t)$ into the above equation and rearranging in terms of curvature yields

$$\alpha V^2(t)=Kk(t)+DL\,\dot{k}(t)+JL\,\ddot{k}(t) \tag{S30}$$

Taking the Laplace transform under zero initial conditions gives

$$\alpha V^2(s)=[K+DLs+JLs^2]k(s) \tag{S31}$$

Therefore, the underwater open-loop transfer function from V^2 to curvature k is

$$G(s)=\frac{k(s)}{V^2(s)}=\frac{\alpha}{K+DLs+JLs^2} \tag{S32}$$

Substituting $\alpha$and Kyields the explicit form consistent with Equation (8) in the main text:

$$G(s)=\frac{k(s)}{V^2(s)}=\frac{\frac{C_D(H^2-H_m^2)}{8hL}}{[E_cI_c+E_b(I-I_c)]+DLs+JLs^2} \tag{S33}$$

To use the proposed underwater second-order dynamic model for control design, an underwater open-loop plant model was implemented in Simulink based on the derived transfer function (Equation (8)) (Supplementary Figure 6). Since the electromechanical actuation moment satisfies $M \propto V^2$, the experimental step voltage input $V(t)$was squared to obtain $V^2(t)$, which was used as the transfer-function input to ensure consistency with the model derivation. The plant output is the curvature $k(t)$, which was converted to the bending angle via $\theta(t)=Lk(t)$for direct comparison with experimental measurements.

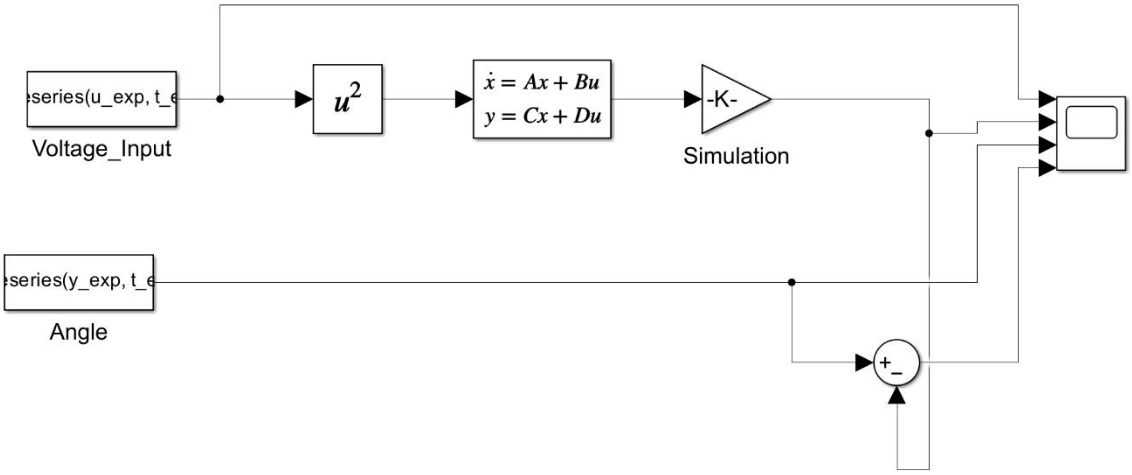

Supplementary Figure 6. Simulink implementation of the underwater open-loop plant based on Equation (8).

The simulation was driven by the same input waveform as in the experiment (0–500 V step voltage). The Simulink-simulated bending-angle response was overlaid with the experimentally measured response for comparison (Figure 4D). It should be noted that the dynamic parameters used here were identified from experimental data; therefore, the purpose of this comparison is to verify whether the proposed low-order model can reproduce the dominant underwater dynamic response characteristics, rather than to provide a high-fidelity independent prediction. The results show that the simulation matches the rising and steady stages well in terms of trend and plateau level, while the discrepancies during unloading are mainly attributed to unmodeled higher-order effects, such as viscoelastic hysteresis, clamping asymmetry, sensor drift, and hydrodynamic nonlinear disturbances. These deviations do not affect the intended engineering use of the model as a control-oriented open-loop plant. In addition, the open-loop step response provides a practical basis for initializing subsequent PID/fuzzy PID controller parameters.

Supplementary Note 9. Initialization and Inference Procedure of the Fuzzy PID Controller

To ensure that the controller gains are initialized in a clear and reproducible manner, the identified plant model G(s) is imported into MATLAB PID Tuner / pidtune, which automatically computes a stable and usable set of baselines PID gains (K_{p0}, K_{i0}, K_{d0}). These gains serve as the “baseline gains” of the fuzzy PID controller, ensuring basic closed-loop stability and controllability in the highly damped underwater environment. On this basis, a fuzzy inference module is introduced to adaptively adjust the gains online, thereby further improving response speed, suppressing overshoot, and enhancing disturbance rejection.

The fuzzy PID controller augments a baseline PID framework with a fuzzy inference module to adjust the PID gains online. The signal flow can be summarized as: error computation → fuzzy inference → gain update → PID output.

1.Error and error-rate computation

$$e(t)=\theta_{\mathrm{ref}}(t)-\theta(t) \tag{S34}$$

$$e_c(t)=\frac{de(t)}{dt} \tag{S35}$$

where θ_{ref} is the reference bending angle and θ is the measured angle from the sensor. In experiments, e_c is obtained using a discrete difference approximation.

2.Fuzzy output and gain update

The fuzzy module takes (e, e_c) as inputs and outputs the gain adjustments (ΔK_p,$\Delta K_i \Delta K_d$) (or equivalent gain update terms). The final PID gains are updated as:

$$K_p=K_{p0}+\Delta K_p \tag{S36}$$

$$K_i=K_{i0}+\Delta K_i \tag{S37}$$

$$K_d=K_{d0}+\Delta K_d \tag{S38}$$

Gain limiting and an anti-windup strategy are adopted to ensure implementability and stability.

To improve the generality and tunability of the rule base, the input variables (e) and e_c are normalized and mapped into a unified universe of discourse ([-3,3]) (schematically shown in Figure 4F):

$$E=K_e e,\ \ \mathrm{EC}=K_{ec} e_c,\ \ E,EC\in[-3,3] \tag{S39}$$

where K_e and K_{ec} are input scaling factors chosen to ensure adequate coverage of the operating data within the universe and to avoid frequent saturation. The output variables (normalized forms of (ΔK_p,$\Delta K_i \Delta K_d$) are also defined over ([-3,3]) and are mapped to physical gain adjustment magnitudes via output scaling factors.

Both inputs and outputs use seven linguistic terms: {NB, NM, NS, ZE, PS, PM, PB}, representing Negative Big, Negative Medium, Negative Small, Zero, Positive Small, Positive Medium, and Positive Big, respectively. Linear triangular membership functions (with shoulder-type behavior at the two ends) are used, with evenly spaced centers at (-3, -2, -1,0,1,2,3). This setting typically yields nonzero membership degrees for only two adjacent terms, enabling smooth inference with low computational complexity.

A Mamdani-type fuzzy inference scheme is adopted. The rule base consists of three 7*7 rule tables: (K_p) (Supplementary Table 7), (K_i) (Supplementary Table 8), and (K_d) (Supplementary Table 9). Each rule is expressed as: IF e is A AND e_c is (B), THEN output is C, where $A,B,C \in \{NB,NM,NS,ZE,PS,PM,PB\}$.

Supplementary Table 7. Fuzzy rules for K_p

e_c e	***PB***	***PM***	***PS***	***ZE***	***NS***	***NM***	***NB***
PB	*NB*	*NB*	*NM*	*NM*	*NS*	*ZE*	*ZE*
PM	*NB*	*NB*	*NM*	*NS*	*NS*	*ZE*	*PS*
PS	*NM*	*NM*	*NM*	*NS*	*ZE*	*PS*	*PS*
ZE	*NM*	*NM*	*NS*	*ZE*	*PS*	*PM*	*PM*
NS	*NS*	*NS*	*ZE*	*PS*	*PS*	*PM*	*PM*
NM	*NS*	*ZE*	*PS*	*PM*	*PM*	*PM*	*PB*
NB	*ZE*	*ZE*	*PM*	*PM*	*PM*	*PB*	*PB*

Supplementary Table 8. Fuzzy rules for K_i

e_c e	***PB***	***PM***	***PS***	***ZE***	***NS***	***NM***	***NB***
PB	*PB*	*PB*	*PM*	*PM*	*PS*	*ZE*	*ZE*
PM	*PB*	*PB*	*PM*	*PS*	*PS*	*ZE*	*ZE*
PS	*PB*	*PM*	*PS*	*PS*	*ZE*	*NS*	*NS*
ZE	*PM*	*PM*	*PS*	*ZE*	*NS*	*NM*	*NM*
NS	*PM*	*PS*	*ZE*	*NS*	*NS*	*NM*	*NB*
NM	*ZE*	*ZE*	*NS*	*NS*	*NM*	*NB*	*NB*
NB	*ZE*	*ZE*	*NS*	*NM*	*NM*	*NB*	*NB*

Supplementary Table 9. Fuzzy rules for K_d

e_c e	***PB***	***PM***	***PS***	***ZE***	***NS***	***NM***	***NB***
PB	*NS*	*PS*	*PB*	*PB*	*PB*	*PM*	*NS*
PM	*NS*	*PS*	*PB*	*PM*	*PM*	*PS*	*ZE*
PS	*ZE*	*PS*	*PM*	*PM*	*PS*	*PS*	*ZE*
ZE	*ZE*	*PS*	*PS*	*NS*	*PS*	*PS*	*ZE*
NS	*ZE*	*ZE*	*ZE*	*ZE*	*ZE*	*ZE*	*ZE*
NM	*NB*	*PS*	*NS*	*NS*	*NS*	*NS*	*NB*
NB	*NB*	*NM*	*NM*	*NS*	*NS*	*NS*	*NB*

During inference, the membership degrees of (E) and (EC) over all linguistic terms are first computed. The firing strength of each rule is obtained using the AND operator, implemented by the commonly used min operator:

$$w=min\big(\mu_E(A),\mu_{EC}(B)\big) \qquad (S40)$$

Multiple rules may point to the same output linguistic term; thus, aggregation is performed using the max operator:

$$\mu_{\text{out}}(C)=max(w_1,w_2,\ldots) \qquad (S41)$$

resulting in the aggregated activation level of each output linguistic term and forming the output fuzzy set for defuzzification.

The center-of-gravity (COG) method is used to defuzzify the aggregated output fuzzy set and obtain a crisp output (Figure 4F). Over the output universe ([-3,3]), discrete sampling is performed. Let the sampling points be z_i, and the aggregated output membership degree be $\mu_{\text{out}}(z_i)$. The defuzzified output is computed as:

$$z_0=\frac{\sum_i \mu_{\text{out}}(z_i)z_i}{\sum_i \mu_{\text{out}}(z_i)} \qquad (S42)$$

To be consistent with the Mamdani inference procedure, the membership function of each output linguistic term is first clipped by its aggregated activation level and then aggregated. For any output linguistic term $L\in\{NB,NM,NS,ZE,PS,PM,PB\}$, the clipped membership function is defined as:

$$\mu_L^{'}(z)=min\big(\alpha_L,\mu_L(z)\big) \qquad (S43)$$

where α_L denotes the aggregated activation level of term L. The overall output membership function is then obtained by max aggregation:

$$\mu_{\text{out}}(z)=max\left(\mu_{NB}^{'}(z),\mu_{NM}^{'}(z),\ldots,\mu_{PB}^{'}(z)\right) \qquad (S44)$$

Substituting μ_{out}(z) into the COG formula yields the crisp output z_0. This crisp output is mapped to the physical gain adjustments $\Delta K_p,\Delta K_i,\Delta K_d$ via output scaling factors and is added to the baseline PID gains to form the final control gains. For numerical robustness, when the denominator $\sum_i \mu_{\text{out}}(z_i)$ approaches zero, the output is set to

Supplementary Note 10. Underwater Durability Test of Rolled Dielectric Elastomer Actuators (DEAs)

The encapsulation test is the same as described in Note S2 2.3. Based on this, several flapping-wing underwater robots were assembled using a fully insulated wound dielectric elastomer (DEA) actuator. The specific assembly steps are as follows: First, a cavity was created using 0.2mm thick FR4 fiberglass board and quick-drying adhesive (GUBAILI G-401) to balance the weight and buoyancy of the underwater robot fish in the water. The assembled underwater robot fish is shown in Supplementary Figure 7B. Subsequently, the underwater robot fish was immersed in water for a durability test (Supplementary Figure 7C). Using a function generator (RIGOL DG1062Z) and a high-voltage amplifier (Aigtek ATA-7020), a voltage of 500 V was continuously applied to both sides of the robot fish at a frequency of 1 Hz, and the swimming performance of the robot fish was observed, as shown in Supplementary Figure 7A. The time from immersion to failure was recorded and summarized in a table (Supplementary Table 10).

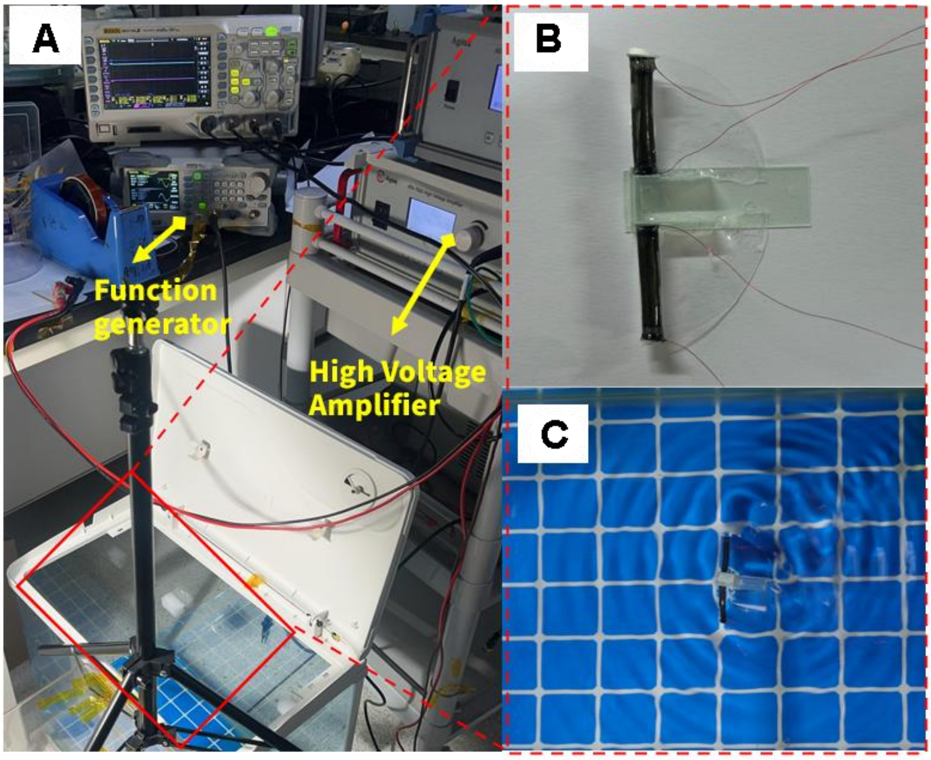

Supplementary Figure 7. (A) Schematic diagram of underwater durability testing environment (B) Completed robotic fish (C) Schematic diagram of robotic fish being launched into the water.

Supplementary Table 10. Underwater Durability Test Results

Device Number	Underwater Effective Operating Time
Device 1	2.6 h
Device 2	3.2 h
Device 3	3.5 h

Test conditions: ZA8LT silicone rubber was used as the dielectric layer. The test conditions were: underwater environment in pure water, room temperature 25°C, sinusoidal voltage 500V@1 Hz.

In this underwater durability test, three prototypes exhibited effective operating times of 2.6 h, 3.2 h, and 3.5 h, with an average of approximately 3.1 h and a small dispersion. These results indicate that the proposed fully insulated encapsulation strategy can maintain stable flapping output under continuous excitation at 500 V and 1 Hz, demonstrating good overall durability[2]. Nevertheless, the final failure of the prototypes may arise from multiple factors: (i) defect accumulation at the encapsulation–electrode interface under alternating high electric fields, leading to increased leakage current or dielectric breakdown; (ii) slight water ingress or edge delamination causing degradation of insulation performance; (iii) fatigue cracking of the electrode/conductive layer under cyclic bending and the associated increase in contact resistance, resulting in attenuated actuation output; (iv) loosening or damage at the cavity–adhesive interface, which alters buoyancy distribution and swimming posture; and (v) electric-field concentration at the lead-out region and sharp edges, potentially triggering partial discharge and premature failure. These failure mechanisms provide guidance for further improving underwater lifetime by optimizing encapsulation materials and sealing processes and enhancing interfacial reliability.

Supplementary Note 11. Estimation of the Effective Ascending Force

During the experiments, the robotic fish was adjusted to a nearly neutrally buoyant state (gravity and buoyancy were approximately balanced). Therefore, in the steady vertical ascending stage, the “effective ascending force” generated by the actuator is mainly used to overcome hydrodynamic drag. Under the assumption of approximately constant-velocity ascent (acceleration ≈0), the force balance yields $F_{\mathrm{ascent}} \approx F_{\mathrm{drag}}$; thus, the measured ascending velocity $v$can be used to estimate the order of magnitude of the effective ascending force. Accordingly, the effective ascending force F_{ascent}can be estimated from the measured ascending velocity $v$using the drag equation:

$$F_{ascent} \approx F_{drag} = \frac{1}{2} C_d \rho S v^2 \tag{S45}$$

Where:

- ρ is the density of water (1000 Kg/m^3).
- S is the characteristic projected area of the robotic fish in the vertical direction (approximately 1.35×10^{-3} m^2based on the prototype dimensions).
- $C_d$is the drag coefficient (approximated as 1.0 for this non-streamlined bluff body structure).
- v is the vertical ascending speed measured in Figure 5B.

Based on the experimental velocity data, the calculated effective ascending forces under different driving voltages are listed in Supplementary Table 11.

Supplementary Table 11. Relationship between Calculated Effective Ascending Force and Driving Voltage

Driving Voltage (V)	**Ascending Speed (BL/s)**	**Ascending Speed (m/s)**	**Effective Ascending Force (mN)**
100	0	0	0
200	0	0	0
300	0.05	0.0015	~0.001
400	0.12	0.0036	0.01
500	0.21	0.0063	0.03
600	0.25	0.0075	0.04

As shown in Supplementary Table 11, the estimated effective ascending force is extremely small (negligible) below 400 V, which explains why no obvious ascent was observed. This indicates that, at low voltages, the cycle-averaged effective thrust is insufficient to overcome hydrodynamic drag and the unsteady resistance during the start-up stage (including added-mass effects). Once the voltage exceeds 400 V, the system enters a stable ascending regime, and the corresponding effective ascending force increases markedly with v. With further increases in voltage and velocity, the estimated force rises significantly, enabling the robotic fish to overcome the quasi-static hydrodynamic resistance and initiate ascent.

References

[1] C. Saracibar. Nonlinear Continuum Mechanics, An Engineering Approach.

[2] Albuquerque FB, Shea H. Influence of electric field, temperature, humidity, elastomer material, and encapsulation on the lifetime of dielectric elastomer actuators (DEAs) under DC actuation. Smart Mater Struct 2021;30:125022. https://doi.org/10.1088/1361-665X/ac3433.